MATERIALS SCIENCE

Laser-engineered heavy hydrocarbons: Old materials with new opportunities

X. Zang[1]*, C. Jian[1,2]*, S. Ingersoll[1], Huashan Li[3], J. J. Adams[4], Z. Lu[1], N. Ferralis[1†], J. C. Grossman[1†]

Polycyclic heavy hydrocarbons (HHs) such as coal, tar, and pitch are a family of materials with extremely rich and complex chemistry, representing a massive opportunity for their use in a range of potential applications. The present work shows that optimal selection of initial HHs based on molecular constituents is essential in tuning the material for a particular and targeted electronic application. Combining the selection of feedstock chemistry (H:C and aromatic content) and controlling variable laser treatment parameters (laser power, speed, and focus) lead to full control over the H:C ratio, sp^2 concentration, and degree of graphitic stacking order of the products. The broad intertunability of these factors results from a wide distribution of carbon material crystallinity from amorphous to highly graphitic and a broad distribution of electrical conductivity up to 10^3 S/m.

INTRODUCTION

Compared to synthetic carbon materials such as graphene and carbon nanotubes (*1*), heavy hydrocarbon (HH)–based materials such as coal, tar, and pitch have rarely been explored as an affordable and abundant material for electronics and optoelectronic applications (*2*, *3*). Yet, through millions of years of evolution in diverse geological environments, the broad chemical and structural heterogeneity in HH provides complex networks of carbon nanostructures with built-in chemical and functional diversity that is currently not taken advantage of. This chemical richness is unmatched but currently untapped given the inability to exploit such diversity as a means to tailor the material properties. A deeper understanding of the relationships between chemical properties and materials functionality for HH alone or when intermixed, along with their tunability in response to materials processing, would allow the harnessing of the potential of HHs as additive feedstocks for the synthesis of materials with customized physical and chemical properties.

Unprocessed HHs are combinations of polycyclic aromatic hydrocarbons (PAHs), alkanes, and sometimes minerals at various concentrations (*4*, *5*). The broad distribution of energy levels and the lack of effective long-range, extended C═C conjugation leads to poor electrical conductivity in HHs (*6*), which can be compensated by bulk annealing to increase conductivity by orders of magnitude through graphitization (*3*). In a traditional quartz tube, annealing temperatures (~1300 K) limit the formation of highly dehydrogenated and crystallized carbon materials such as carbon fibers, graphite, and diamond (*7*). Low heating rates limit the exploration of fast pyrolysis of PAHs at different heating rates, which could provide different structures and properties. The hydrocarbon conversion dynamics during pyrolysis in a conventional tube furnace is relatively slow compared to the same process using laser ablation. The main difference can be accounted in the desorption of lighter hydrocarbons during the heating ramp, with the temperature of the material not sufficiently high to reincorporate them into the residual, heavier carbon matrix. With laser ablation, the rapid heating rate to graphitization temperatures leads to almost immediate incorporation with lower material loss (~50%) compared to conventional furnace annealing (with mass loss >80%) (*7*). Hence, laser ablation allows the exploration of fast pyrolysis, with controlled material loss. Furthermore, bulk annealing methods do not lend themselves to spatially control the heating process, and they require the supporting substrate to be able to sustain the same annealing temperature as the film. State-of-the-art methods to manufacture such carbon materials from HH feedstocks require much higher temperatures and complex carbonization processes [i.e., highly graphitic and interconnected carbon fiber made from coal mesophase (MP) pitch requires T ~2500° to 3000°C (*8*)]. Laser ablation offers a combination of benefits for such purposes, including the rapid, extremely localized heating up to T ~3000°C at low incident power (2 W) (*9*, *10*), enabling selective carbonization/graphitization in ambient environments while maintaining the substrate near room temperatures, allowing for the use of soft substrates. In processing carbonaceous materials, tuning the annealing processing conditions is usually the preferred method to fabricate graphitic materials with desired performance properties. However, this method often underscores the role played by the initial carbon source as the primary determining factor of the resulting material properties, given similar processing conditions. In this work, we will show that structural and functional chemistry within the heterogeneous HH mix of the initial carbon source (in particular, the aromatic, aliphatic, and heteroatom concentrations) greatly affects the structure and performance of the resulting carbon films, such as porosity and electrical conductivity. Using proper feedstock selection before ablation allows the ultimate fabrication of a carbon materials with specific characteristics imposed at the time of fabrication with spatial control.

RESULTS AND DISCUSSIONS

A CO_2 laser is used as a means to tune the chemistry, morphology, and conductivity of HHs, including petroleum steam cracked tar, low-volatile bituminous (LvB) coal, and MP pitch and their mixtures (Fig. 1, A and B) (*11*). Tar, coal, and pitch are chosen as representative HH materials because of their wide-ranging H:C ratio, aromatic content, and initial structural alignment (*12*, *13*). Tar has the highest H:C and more alkane content than MP and coal (*12*). MP is a thermotropic

[1]Department of Materials Science and Engineering, Massachusetts Institute of Technology, Cambridge, MA 02139, USA. [2]Department of Mechanical Engineering, York University, 4700 Keele Street, Toronto, ON M3J 1P3, Canada. [3]School of Physics, Sun Yat-sen University, Guangzhou 510275, China. [4]Western Research Institute, Laramie, WY 82072, USA.
*These authors contributed equally to this work.
†Corresponding author. Email: jcg@mit.edu (J.C.G.); ferralis@mit.edu (N.F.)

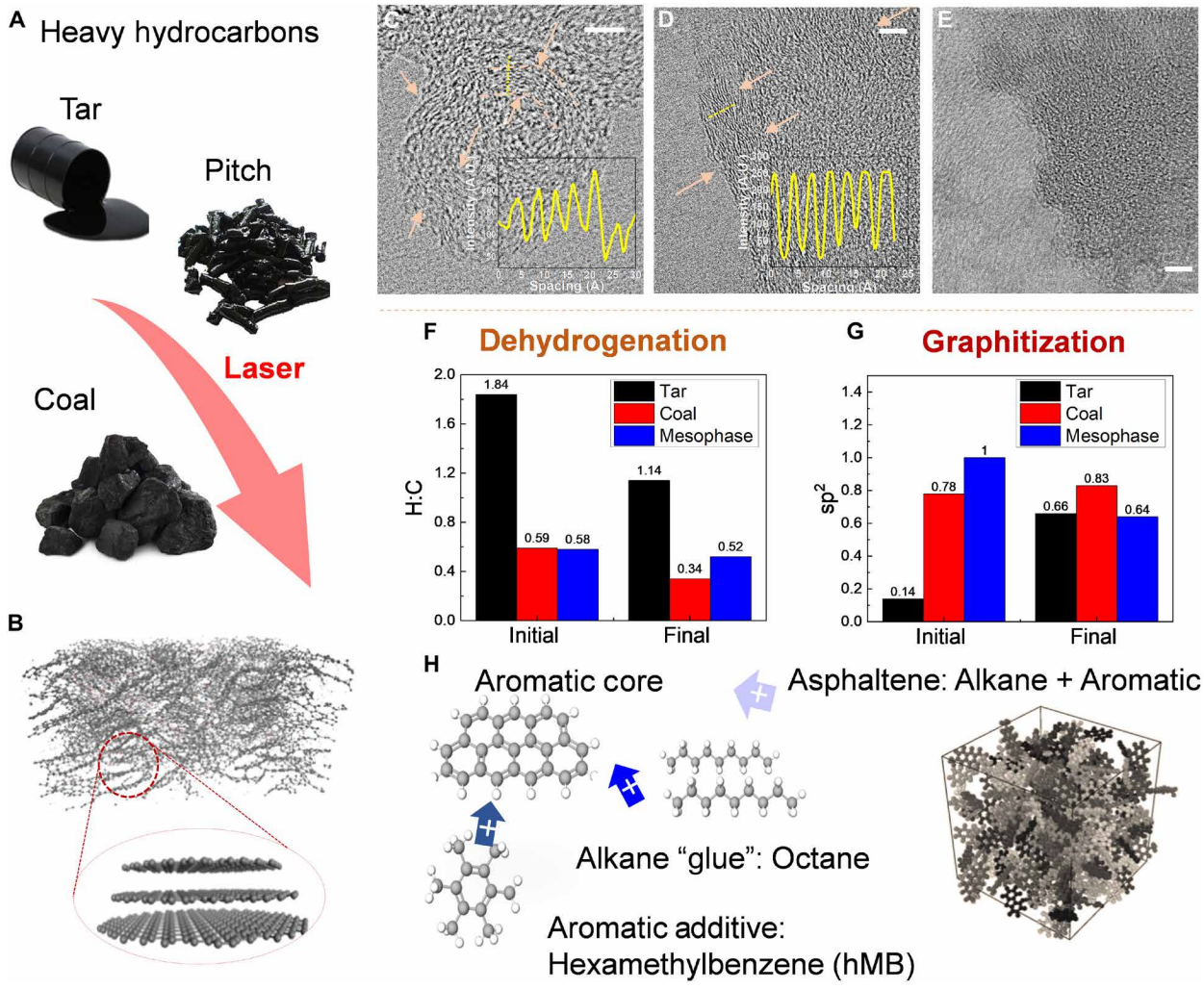

Fig. 1. Schematic of laser ablation of natural HH (coal, MO pitch, and tar). (**A**) HH materials: tar, MP, and coal. (**B**) Laser-ablated stochastic graphitic system from HH. (**C**) TEM image of laser-ablated steam cracked tar. (**D**) TEM image of laser-ablated LvB coal (DECS 19). (**E**) TEM image of laser-ablated MP pitch. Arrows point to graphitic fringe stackings. Scale bars, 5 nm (C to E). Insets of (C) and (D): Profiles of highlighted lines. The average interlayer spacing of ablated tar is ~4.3 Å, and that of ablated coal is ~3.4 Å. (**F**) MD simulation result of sp^2 carbon change in tar, coal, and pitch after laser ablation. (**G**) MD simulation results of H:C ratio change in tar, coal, and MP pitch after laser ablation. (**H**) Schematic of how naturally occurring PAHs are stitched to larger graphitic clusters when ablated by CO_2 laser. A.U., arbitrary units.

crystal from pitch processed at low temperature, where isotropic pitch is polymerized into higher molecular weight components with a high degree of aromatic structural order (*14*). MP has the lowest H:C and highest aromatic content with aligned aromatic sheets (fig. S1) (*15*, *16*), while LvB (Department of Energy Coal Sample 19, as selected in this work) coal has the largest initial aromatic core, intermediate H:C ratio and aromatic content (*17*). Benefiting from the understanding of the materials properties from each feedstock in combination with the high-temperature, highly localized thermal treatment provided by the laser provides an opportunity to develop customized carbon materials and their scalable and additive deployment in electronics.

Fourier transform infrared (FTIR) spectrum of laser-ablated coal, tar, and MP pitch is reported in fig. S2 (A and B). The CO_2 laser wavelength is 10.6 μm, corresponding to 940 cm^{-1}. The peaks around 940 cm^{-1} indicate bending modes of aromatic C—H, which show similar fingerprints on the spectrum of tar, coal, and pitch. With the carbon numbers increasing from 10 to 60, total integrated IR absorption cross section of PAH from 10 to 15 μm only slightly decreased by <12% (*18*). Within the range of 20 to 30 carbon atoms, the IR total absorption cross sections of PAHs only slowly drop less than 5% (*18*). Meanwhile, the absorption intensity is affected by the molecular orientation and film structure such that the spectrum intensity cannot be used to quantify the CO_2 laser absorption (*19*). However, given the heterogeneous distribution of aromatics, the most substantial contribution to the absorption derives from the larger clusters in the HH mixtures, allowing mixtures rich in small aromatic to be processed with excitation light usually more suitable for mixtures rich in larger aromatics (*20*). We tested different laser parameters for optimized conductivity. Characterization of materials reported in the paper is performed on the ablated product with the best conductivity. The broad structural diversity of the carbon products formed from laser-ablated HHs is shown by high-resolution transmission electron microscopy (HRTEM) images (Fig. 1, C to E). TEM images are performed on multiple (>10) sample spots, and additional TEM images are shown in fig. S3. In the case of tar, laser ablation leads

to nanoscale (~5 nm, size of scale bar) graphitic fringes mediated with amorphous carbon, similar to carbon black or soot with paracrystalline graphitic domains and amorphous hydrocarbons (*21*). Laser-ablated LvB coal shows larger graphitic fringes and domains (>30-nm lateral size) and over 10 layers of stacking, indicating increased graphitic sheets and a higher level of graphitization. The interlayer spacing between graphitic sheets extracted from line profiles of TEM images from ablated tar and coal are 4.3 and 3.4 Å, respectively (Fig. 1, C and D). Laser-ablated MP results in small fragments (dark in contrast, smaller than a scale bar size of 5 nm) without obvious stacking or fringes. Raman spectra (Fig. 2A) support the HRTEM images, with the two-dimensional (2D) (2750 cm^{-1}) peak sensitive to pi-stacking largest in ablated LvB coal, smaller in ablated tar, and non-existent in ablated MP (*22*). Ablated LvB coal also shows a sharper G (1580 cm^{-1}) peak in the Raman spectrum indicating a larger sp^2 cluster (crystalline) size compared with tar (*23*), while the ablated MP has the broadest D (1350 cm^{-1}) peak and highest I_D/I_G ratio, suggesting smaller sp^2 cluster sizes and larger disorder (*24*).

Molecular dynamics (MD) simulations are performed to reveal the dehydrogenation and graphitization evolution of HH annealed at 4000 K (Fig. 1, F to H). Model and simulation parameters can be found in the Supplementary Materials (fig. S4 and table S1). It should be noted that it is challenging to identify specific HH species given the broad distribution of potential isomers in tar, coal, and pitch. Thus, for the simulations we used a previously proposed approach where an ensemble of typical representative compounds is selected to mimic the overall key chemical features of the HH feedstocks (*25*). The tar model is built by packing aromatic molecules with aliphatic chains with H:C ratios and aromatic contents reflecting the measured values (*26*). The MP model is built using polycyclic aromatic molecule that matches the H:C ratio (0.46) of the provided feedstock, as shown in the Supplementary Materials. The coal model is built by packing a typical molecule fragment for corresponding measured density and H:C ratio (*27*). In this work, we selected H:C ratio and aromatic content as the key structural descriptors of the feedstock, because it has been proposed that these two factors affect properties of final products under high-temperature treatment (*28*). We primarily focused on the chemical evolution of molecular models for coal, tar, and pitch generated by packing the most representative molecules with corresponding H:C ratio and density

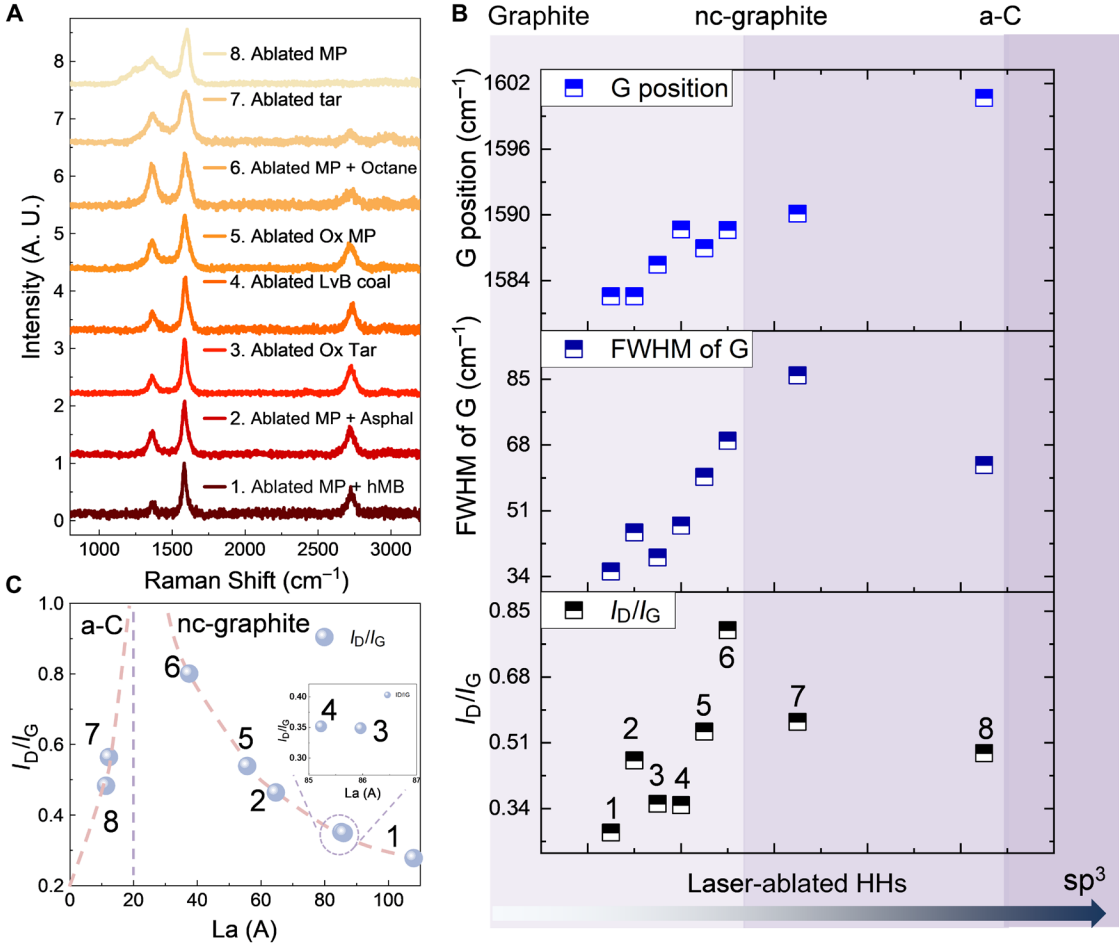

Fig. 2. Raman analysis of HHs, oxidized HHs, and laser-ablated HHs. (**A**) Raman spectrum of laser-ablated HHs. Raman spectrum of laser-ablated MP with different additives. The increased 2D peak and narrowed G peak indicate a better aromatic stacking in laser-ablated MP with additive alkane and small aromatic fragment. Raman spectra of laser-ablated oxidized tar and MP thin films showing a strong 2D peak compared to the near-zero 2D peak in ablated nonoxidized films. (**B**) I_D/I_G ratio, FWHM, and G peak position analysis of Raman spectra. The numbers in each data point indicate a different sample. Ox, oxidized; Asphal, asphaltene; a-C, amorphous carbon; nc, nanocrystalline. (**C**) Fitted in-plane crystallite size L_a from I_D/I_G.

(table S1 and fig. S4) (*6*, *29*, *30*). The initial H:C ratio (1.84) in tar leads to a more substantial dehydrogenation and increase in the sp^2 content when ablated (0.66). Coal with larger aromatic cores, intermediate H:C ratio (0.59), and intermediate initial sp^2 (0.78) produced the highest sp^2 content (0.83) and highest graphitic stacking reflected from the peak in the radial distribution function (fig. S5). In the case of MP, the highest initial sp^2 ratio (~1.00) and aromatic content lead to even lower graphitic stacking (fig. S3D) and sp^2 ratio (0.64). Furthermore, the H:C ratio in MP only slightly decreased from 0.58 to 0.52 when heated to 4000 K in the MD simulations. In this case, the difficulty of dehydrogenation and lack of alkane chains leads to the thermal energy destroying the original aromatic structures and a corresponding decrease in sp^2 carbon. The simulated sp^2 ratio change in laser-ablated HHs shares the same trend of sp^2 carbon in the x-ray photoelectron spectra of HHs in fig. S5. The sp^2 carbon ratios in tar and coal both slightly increase from 0.74 to 0.81 and from 0.76 to 0.88. We note that sp^2 carbon in the MP x-ray photoelectron spectroscopy results before and after ablation substantial decreases. The carbon 1s spectrum peak also shifts to an asymmetric shape in the ablated MP. These simulation results suggest that both alkane chains and built-in large aromatic cores are crucial to "stitch" the original aromatics in the HHs together and induce graphitic stacking (Fig. 1H). The role of alkane chains is to supply carbon to the original aromatic sheets by dehydrogenation, which we further illustrate by adding octane to MP in the experiments, which leads to an increased 2D peak in the Raman spectrum (Fig. 2A) (*22*). In addition to alkane, addition of small aromatic molecules [hexamethylbenzene (hMB)] further increases the sp^2 cluster size and graphitic stacking (Fig. 1H). Asphaltene, an isotropic PAH with extensive alkane edge functionalization (*31*), acts as a highly effective additive to MP to induce extended graphitic structure when laser-ablated (Fig. 1H).

Alternatively, oxygen-induced cross-linking of aromatic clusters can be obtained through low-temperature annealing in an oxygen-rich environment. This process is essential during production of pitch-based MP carbon fibers, where extended graphitic domains are formed during oxidation and subsequent carbonization and graphitization (*8*). The oxidized tar thin film (300°C, in air, 4 hours) shows a Raman fingerprint with polyaromatic features (fig. S2C) in contrast to the fluorescent broad band in nonoxidized tar. All Raman spectra of laser-ablated HHs are summarized in Fig. 2A, with the consideration of G peak position, full width at half maximum (FWHM) of G peak, I_D/I_G ratio, and the presence of 2D peak. Laser-ablated HH falls in the microcrystalline/nanocrystalline (mc/nc) graphite and amorphous carbon regimes (Fig. 2B), and the transition of Raman signature between different crystalline structures can be found in (*32*). Laser-ablated MP and tar fall in the amorphous carbon regime, and laser-ablated coal and MP with other additives all fall in the mc/nc graphite category. We also estimate the graphitic crystallite size L_a of laser-ablated HHs (Fig. 2C) (*24*). In the amorphous carbon regime, I_D/I_G is proportional to the square of the square of L_a. In the nc-graphite regime, I_D/I_G is proportional to the inverse of L_a (*24*, *33*). With the decrease of graphitic structure, the G peak shifts from ~1580 to ~1590 cm^{-1}. Laser-ablated MP with additive hMB shows the lowest I_D ratio, G peak wave number at ~1582 cm^{-1}, and smallest FWHM (~34 cm^{-1}), indicating the highest graphitization level and the largest graphitic crystallite size. Laser-ablated MP with asphaltene and octane shows an increase of I_D/I_G, FWHM, and G peak position. Such results support the idea that the extension of graphitic structure favors the presence of both alkane and aromatic additives. It has to be noted that although the G peak position of ablated MP with asphaltene shows the lowest G peak position (~1581 cm^{-1}) and highest 2D peak, the I_D/I_G ratio increases with a broadening of the FWHM. Our hypothesis is that with the extensive alkane-attached PAH, the ablated MP and asphaltene formed highly graphitic structures. However, the competing growth and graphitization of large aromatic sheets in both MP and asphaltene broadened the distribution of aromatic size and the width of the D peak.

Low-temperature oxidation of MP thin films (300°C, in air, 4 hour) results in a strong 2D peak in Raman (Fig. 2A) after laser ablation and 2.36 times higher electrical conductivities than the nonoxidized laser-ablated MP pitch. Oxidized tar provides over 36 times higher electrical conductivity after laser ablation than nonoxidized laser-ablated tar (Fig. 3A). The boosted conductivity and 2D Raman peak in oxidized tar and MP indicate a substantially higher degree of

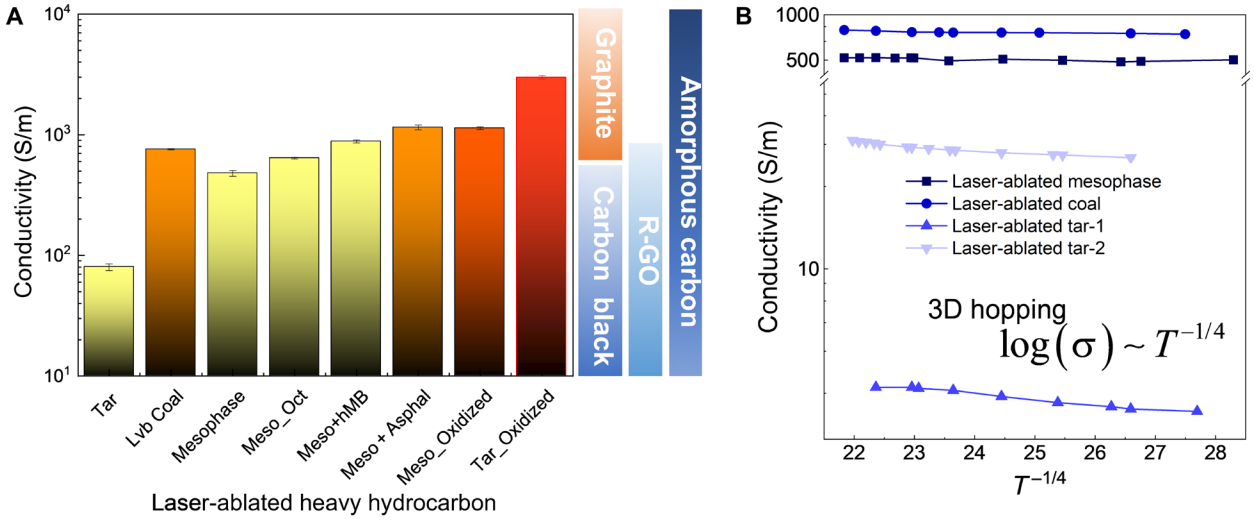

Fig. 3. Conductivity and electrical transportation of HH. (**A**) Conductivity of laser-ablated natural polyaromatic hydrocarbon (NPAH) thin films and their hybrid thin films compared to the conductivities of synthetic carbon materials. (**B**) Temperature-dependent conductivity of laser-ablated NPAHs.

conjugation and stacking between aromatic sheets (Fig. 2A). The nc-graphitic crystallite size derived in Fig. 2C is positively correlated to the conductivity in Fig. 3A. Laser-ablated oxidized tar with large graphitic size shows higher conductivity (~2990 S/m) than laser-ablated oxidized MP (~1133 S/cm). The understanding of the functionality of each component of HHs provides guidelines to tune the morphology (fig. S6, A and D) and conductivity of as-ablated products by optimizing the composition of the heterogeneous mixtures of HH feedstocks and laser processing parameters. Ablated tar is composed of sub–100-nm–size carbon black particles, while ablated coal shows a stochastic hierarchical nanoporous structure formed by the merging of initial discrete coal particles (fig. S6B, inset). The higher graphitization of ablated LvB coal leads to an order of magnitude higher conductivity (~800 S/m) compared to ablated tar (~80 S/m) (Fig. 3A), while the poorly graphitized ablated MP still shows a large conductivity (~500 S/m) due to its interconnected structure (fig. S6C and Fig. 3A). The presence of molecular bridges can greatly increase the charge transfer and electron coupling, which in turn can enable conductivities similar in magnitude to graphite-like networks. Such phenomena have been discussed extensively in previous paper (*6*). By tuning the laser ablation parameters, the conductivities of HH thin films can be tuned over three orders of magnitude using tar as an example. By controlling the initial HH selection and additive agents like hMB and asphaltene, the conductivities of HH thin films can be increased from below 100 to ~1000 S/m. Together, these results indicate that laser ablation using HHs as a chemical tool box produces a broad variety of carbon materials comparable to carbon black, amorphous carbon, and graphitic carbon (Fig. 3A and table S2) (*34*, *35*).

Although ablated LvB coal and MP provide higher conductivities, ablated tar shows a temperature-dependent hopping behavior and a broader range of tunability (Fig. 3B). Tar, made of smaller non-interconnected units and with higher aliphatic content MP and coal, makes it more mobile from a rheological perspective. This offer more degrees of freedom and therefore more tunability to reordering, and the ablated tar conductivity shows a Mott-like $\log(\sigma) \sim T^{-1/4}$ relationship, indicating intermolecular connection and extended conjugation (*6*). Coal and MP, on the other end, are less tunable, more structurally rigid, and with lower aliphatic content, but have larger clusters and therefore more stacking. This leads to more sites where new conjugate bonds can form, leading to higher conductivities. The CO_2 laser can generate high localized temperatures with relatively low incident power (1.6 to 4.8 W; Fig. 4 and fig. S6A) (*36*), enabling carbonization of the tar film in an ambient environment. FTIR spectra are consistent with the MD simulations (Fig. 1F and fig. S7B), showing a significant decrease of C─H bonds (3000 cm^{-1}) and increase of C─C bonds (1000 cm^{-1}) in the ablated tar films (fig. S7, C to F) (*37*). Parameter optimization including power, laser rastering speed, and focus are detailed in Fig. 4. The optimized tar films in this case (~80 S/m) are achieved with 14% of full power (4.2 W), 0.08-inch defocusing, and 127 mm/s scanning speed (Fig. 4A). Aromatic content evolution and dehydrogenation of tar during laser ablation can be analyzed by optical absorption spectra (Fig. 4, B to D) (*7*, *20*), which reveals an aromatic/aliphatic ratio increases from ~0.35 to ~0.55 and an H:C ratio decrease from ~1.20 to ~0.95 (Fig. 4D) (*20*). The increase of power increases the 2D peak (Fig. 4E), indicating graphitic stacking induced by the higher annealing temperature. Figure 4F shows a near-linear trend of the power/defocus ratio; at each defocus, the highest conductivity can be achieved using a fixed scan speed. Such a trend can also be observed from the optical image in Fig. 4A, in which the dashed line indicates the evolution of best conductivities. Below the power/defocus optimized ratio, an increase of power prompts the dehydrogenation to increase conductivity. Above the optimal ratio, high laser power blasted the tar thin film away, leaving conductivity.

Prototyping HH-based conductive features require a set of simple steps (Fig. 5A and Supplementary Materials): HH film spincoating, laser printing of electrodes, residual HH stripping, and further transfer process for the case of flexible devices. When used to fabricate electronic devices, coal thin films suffer from high surface roughness induced by loose particles with tens of nanometer sizes due to milling limitations (*3*); its use, however, can be beneficial as an electrically conductive porous membrane. MP and its mixtures with alkanes and asphaltene are difficult to strip due to low solubility in *N*-methyl-2-pyrrolidone (NMP), requiring elevated temperatures that could potentially harm a printed device. While these are not insurmountable drawbacks, for demonstration purposes in this work, we use tar due to its processability in solution and facile stripping. Conductive tar lines (with resolution of ~25 μm in this case) can be patterned with tunable line spacing corresponding to different transparency and resistivity (Fig. 5B). Transparent heaters made from laser-ablated tar show remarkably high-temperature performance (fig. S8) with 40% transparency, with 400°C at 60 V (*7*), outperforming silver nanowire heaters that typically fail over 200°C and using inexpensive, highly abundant HH when compared with synthetic materials such as single-wall carbon nanotubes (*38*). The high electrical conductivity in devices fabricated from ablated tar and other films made from HHs could allow them to be implemented in energy storage microdevices with performance competitive with current state of the art (Fig. 5B and fig. S8). Ablated tar thin films can be transferred to soft substrates like polydimethylsiloxane (PDMS) for flexible devices such as strain sensors (Fig. 5, C to E, and fig. S8). Compared to the laser-ablated tar strain sensor, other laser-ablated HHs such as the MP/asphaltene composite provide a lower gauge factor but much higher conductivity. These three different device architectures suggest the broad engineering possible for a variety of target properties, taking advantage of the complexity of chemistry and richness of candidates in the HH toolbox.

CONCLUSION

In summary, by controlling the processing and environmental parameters during laser annealing of selected HH feedstocks, we demonstrate a wide tunability of ablated product properties, spanning a range of crystalline structures, conductivities, and electron transport mechanisms. The optimal conductivity and structural stability from engineered molecular alignment allow the fabrication of these devices. In essence, leveraging the work done by nature in customizing the chemistry and structure of different HH, the carbon films are engineered to achieve the required level of performance at the device-level, using simple materials processing. The development of low-cost processing methods in this work provides a path toward scalable and inexpensive manufacturing of devices made from HH feedstocks as either the active layer directly or additives with a host of potential applications.

MATERIALS AND METHODS

Materials

Stream cracked tar was provided by ExxonMobill (Defluxed SOP2 Tar from 15-082837). LvB coal (Pocahontas #3 Seam, Buchanan County,

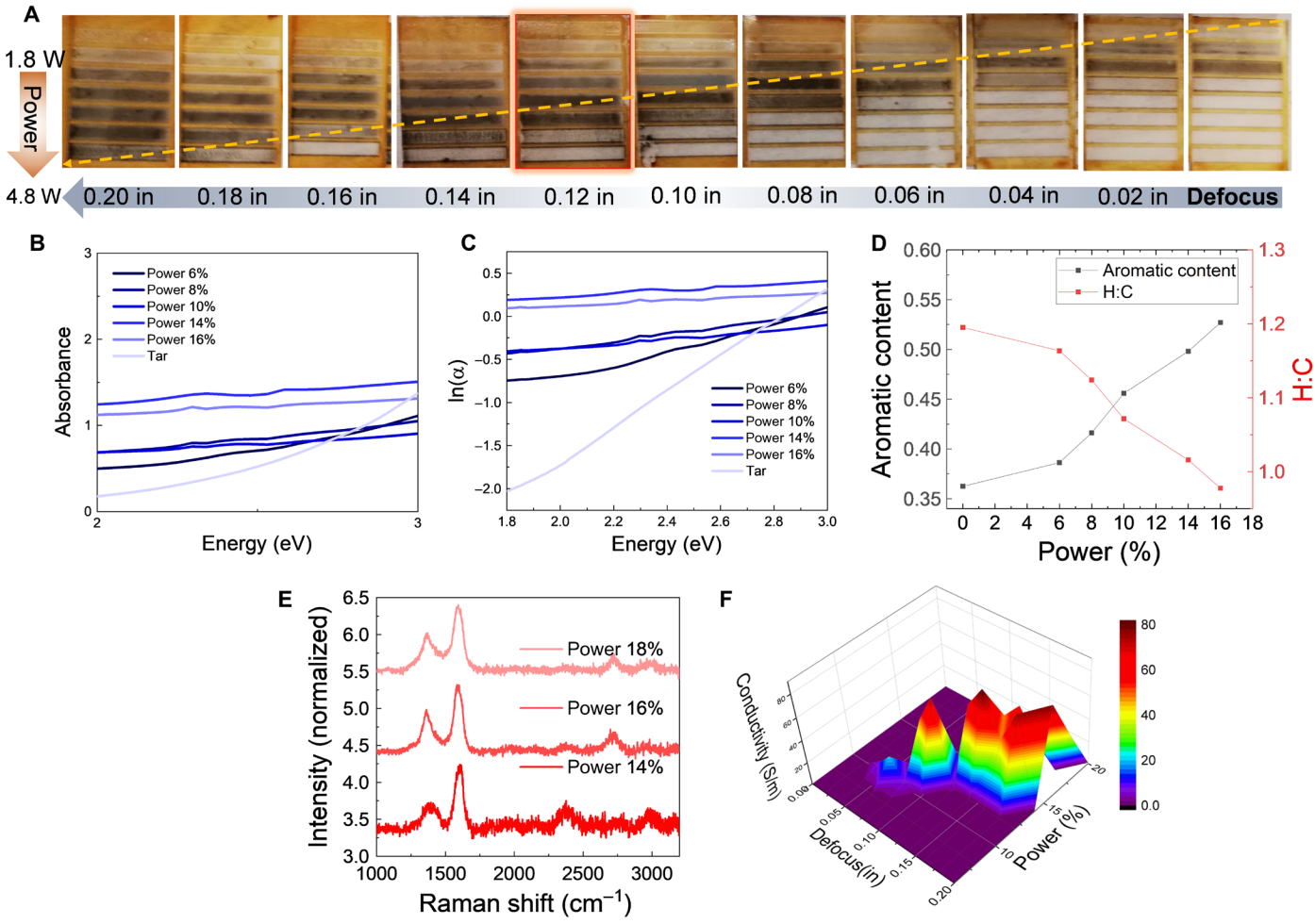

Fig. 4. Conductivity optimization of laser-ablated tar. (**A**) Optical images of laser-ablated tar thin film. The scanning speed is fixed at 127 mm/s, while defocus and laser power vary as labeled on the image. Optical absorption analysis of laser-ablated tar. Photo credit: Xining Zang, Massachusetts Institute of Technology. (**B**) Visible light (2 to 3 eV) absorption of tar and ablated tar, from which Urbach tail is derived in (**C**). The slope of (B) can be used to derive H:C ratio and aromatic content following the method in (*20*). (**D**) H:C ratio and aromatic content change in response to different laser power at the same defocus setting at 0.14 inches. (**E**) Raman spectrum of laser-ablated tar with different power at a defocus distance of 0.14 inches. (**F**) Conductivities of ablated tar, which shows a tentative linear response to power/defocus. In (E) and (F), the full-range power is 30 W. Percentage is used to record the parameter tuned in the software interface. The real power numbers can be calculated accordingly.

VA, DECS 19) was from the Department of Energy Coal Bank hosted at the Pennsylvania State University (*39*, *40*). Two kinds of solvent, NMP (CAS 872-50-4) and dichloromethane (CAS 75-09-2), were purchased from Sigma-Aldrich. MP pitch (CTP 6-SP 147, MP Rx 11/20) was provided by J. Adams from Western Research Institute, with a softening point at 333.5°C and H:C ratio of 0.46.

Methods

Thin-film deposition

Tar was dissolved in dichloromethane (DCM) to make a 60 weight % solution. The tar solution was spin-coated onto glass at a speed of 2000 rpm for 20 s. MP pitch is diluted in NMP at elevated temperature up to 150°C. The MP suspension is spin-coated onto a glass slide at a speed of 500 rpm for 20 s. The MP thin films is annealed in air for 4 hours at 300°C to prepare oxidized MP thin films. LvB coal powder is dispersed in DI (distilled water) with 9:1 mass ratio to make a granular suspension and drop-casted onto glass slide. Each tar, MP, and coal thin film deposited onto glass was dried in air and heated up to 80°C to remove volatile content.

Laser ablation of tar, coal, and pitch

A commercial Universal VSL 2.30 was used to perform the laser ablation, with a CO_2 laser tube (maximum power of 30 W) and all built-in optics. The laser spot is focused on the top surface of spin-coated films, and the height of the sample is controlled by tuning the *z*-position of the supporting cutting table. The designed device pattern is imported to a vector graphics software (Inkscape) and engraved by communicating with the laser cutter as a printer. Unablated tar, pitch, and coal can be easily removed by rinsing the whole device in NMP, DCM, and DI water separately for 1 min and air-dried before testing.

Materials characterization

A profilometer (Bruker DXT Stylus Profilometer) was used to map the thickness of spin-coated and laser-ablated thin films [scanning electron microscopy (Hitachi SU8100)]. A TEM (JEOL 2011 High Contrast TEM) was used to study the morphology and structure. XPS (Thermo Scientific K-Alpha XPS) was used to study the surface element component of samples. The Al Kα micro-focused monochromator has a variable spot size of 30 to 400 μm in 5-μm steps. The grazing incident wide-angle x-ray scattering (WAXS) experiments

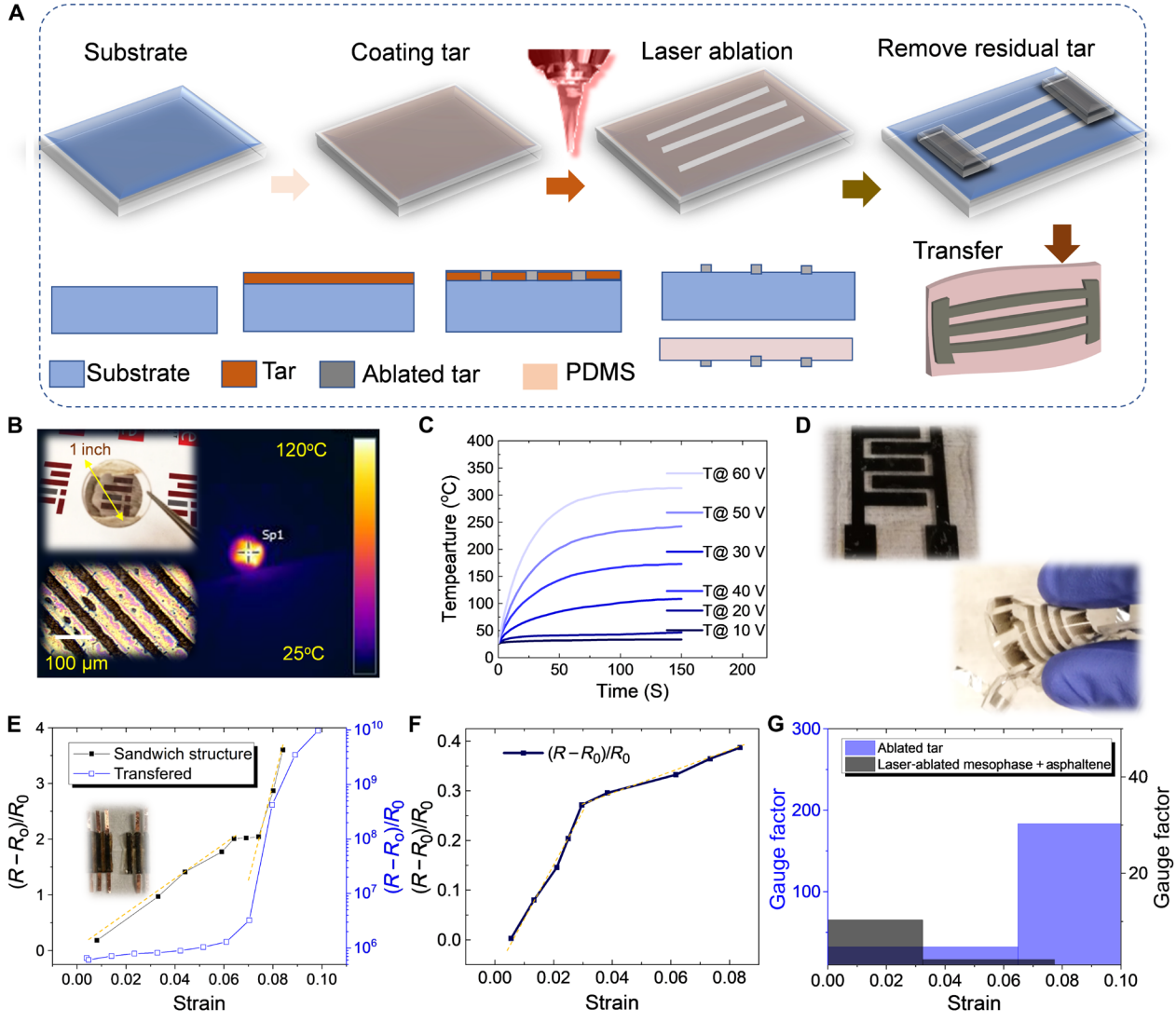

Fig. 5. Applications of laser-treated tar in electronics and additive manufacturing. (**A**) Fabrication schematics of laser-printed devices, including patterning, washing, and transfer process. (**B**) Laser-printed tar-based devices including a transparent heater, an interdigit supercapacitor, and a flexible strain sensor transferred onto PDMS. Details of performance are shown in the Supplementary Materials. (**C**) Heating responses under different bias. Temperature will plateau after ~20 s, and the saturated temperature increases with input bias voltage. Heating temperature can reach up to 300°C under 60-V bias. (**D**) Optical image of laser-printed supercapacitor and strain sensor. (**E**) Performance of strain sensor made of laser-ablated tar. (**F**) Performance of strain sensor made of laser-ablated MP-asphaltene composite. (**G**) Comparison of gauge factors of strain sensor in (E) and (F). Photo credit: Xining Zang, Massachusetts Institute of Technology.

were performed with a Pilatus3R 300K detector using the Bruker NanoStar small-angle x-ray scattering diffractometer on top of a Rigaku H3R rotating anode generator (x-ray diffraction spectrometer at the Material Processing Laboratory at the Massachusetts Institute of Technology). A small-angle 2-mm beam stop with a sample detector of 109.1 mm was used for WAXS measurements. The exposure time was set as 300 s. Raw WAXS patterns were processed with corrections by MATLAB-based GIXSGUI software before analysis. Micro-Raman spectra were acquired using a Renishaw inVia confocal Raman microscope using a 473-nm excitation source. The laser spot on the sample was ~800 nm in diameter and had a power of ~4 mW at the sample surface. The full spectral window for each acquisition is from 600 to 3200 cm^{-1}. Optical absorption spectroscopy was performed with an Agilent Carry 60 ultraviolet-visible (UV-vis) spectrometer over the range of 1100 to 200 nm. Attenuated total reflected (ATR) IR spectrum was mapped on the surface of tar thin film on the non-ablated and ablated regions using a Bruker FTIR microscopes in contact mode.

Conductivity and temperature-dependent conductivity measurement

A lakeshore TTP4 probe station with liquid N_2 cooling was used for the low-temperature characterization. The parameter analyzer (4156C) is interfaced with a PC running EasyExpert software to set up any test with up to 1 mA and 5 V. All room temperature electrical characterization was done in air, and all low-temperature characterization was done under vacuum.

MD simulation

The initial configuration of each sample was first generated by packing the corresponding concentrations of molecules (system compositions shown in table S1 and fig. S4) into a rectangular box. Then, dynamic

equilibration was performed in the NPT ensemble at 300 K and 1 bar for 1 ns to fully relax the system to a density close to an experimental value: 0.89 g/cm^3 for tar, 1.41 g/cm^3 for coal, and 1.23 g/cm^3 for pitch. The H:C ratio is the highest in tar, higher in coal, and the least in pitch (*12*). To further align MP, where the orientations of molecules are anisotropic, uniaxial tensile stretch was applied to the pitch system, with an ultimate strain of 100%. The aforementioned systems were then gradually heated from 300 to 4000 K (heating rate, 0.125 K/fs) in the NVT ensemble and subsequently subjected to constant temperature dynamics for 300 ps. Reactive potentials from the work of van Duin *et al.* (*41*) on coal were adopted to describe interatomic interactions, and to account for polarization effects, charge equilibration is performed to adjust the partial charge on each atom. During these high-temperature simulations, the time step was 0.1 fs; temperature was maintained using a Nose-Hoover thermostat. For all simulations performed using LAMMPS (*42*), VMD (*43*), and Vesta (*44*) were used for visualization.

Given the time scale difference between experiments (~200 μs) and simulations (300 ps), the temperature here is scaled using Arrhenius equation to increase the reaction rate in simulations. That is, the temperature adopted in our simulations is not directly comparable to that in experiments. In Arrhenius equation, the dependence of the rate constant of a chemical reaction on the absolute temperature is given by

$$k = A\, e^{(-E_a/RT)}$$

where k is the rate constant (units depending on specific reactions), T is the absolute temperature (K), E_a is the activation energy (in the same units as RT), and A is the pre-exponential factor (in the same units as k). Taking pitch molecules as an example, its activation energy is reported to be from 140 to 190 kcal/mol

$$\frac{k_r}{k_s} = e^{-\frac{E_a}{R}\left(\frac{1}{T_r}-\frac{1}{T_s}\right)}$$

$$\ln\frac{k_r}{k_s} = -\frac{E_a}{R}\left(\frac{1}{T_r}-\frac{1}{T_s}\right)$$

k_r denotes the reaction rate in experimental real time, and k_s denotes the reaction rate in simulation time. The reaction rate is reverse to the reaction time scale. T_r denotes the reaction temperature in experimental real time, and T_s denotes the reaction temperature in simulation time. The reaction rate is reverse to the reaction time scale. Using E_a = 170 kcal/mol, we estimate the corresponding temperature in real time scale and simulation time scale. The laser-induced temperature should be above 2000°C, but below the degradation temperature of graphite ~3000°C. From (*9*, *10*), the laser-induced temperature is roughly estimated at 2500° to 3000°C. As such, we choose 4000 K to perform the simulation.

Optimization of laser ablation of tar thin film

Compared to ablation in air, ablated tar with N_2 purging shows no significant difference in conductivity and in the ATR spectrum on selected spots of ablated areas (fig. S7), which can be attributed to the reducing atmosphere decomposed from H-C by the laser power (fig. S7). At focus, laser-ablated tar using different power and speed are crossed compared for maximum conductivity. In addition to changing the laser power and speed (Fig. 4), the beam can be spread by defocusing to decrease energy density, which can improve the uniformity of the resulting film (*45*). With fixed speed (127 mm/s), the laser power and defocusing are varied (Fig. 4). The bright orange line indicates the near-linear relation of power/defocus ratio that leads to highest conductivities (Fig. 4). Settings with higher power/defocusing result in higher mass loss of electrodes with poor conductivity, while the electrodes ablated with lower power/defocusing ratio also suffer low conductivity due to residual hydrocarbons.

Prototyping tar-based electronic devices

Tar thin films are deposited as described above. Calibration of laser parameters resulting in highest conductivity was first performed. With a computer aid design interface, many features can be directly printed on tar film. As-ablated devices were rinsed in solvent DCM to remove the unablated areas and air-dried followed by heating up to 100°C to fully remove the solvent.

Optical absorption spectroscopy measurements

Optical UV-vis absorption was carried out in reflectance mode on solid-state samples (*9*). The optical absorption of HH and laser-ablated HH reveals more information of their aromatic/aliphatic ratio (H:C ratio). Urbach tail E_0 derived from optical absorption $\alpha(\omega) \sim \exp(\hbar\omega/E_0)$ unlocks the information of H:C ratio and aromatic content, which are two key factors for the conductivity of carbon materials (*20*).

Fitting I_D/I_G for in-plane crystallite size La

Peak intensity ratio of D and G peaks (I_D/I_G) has been used to estimate the cluster size of carbon using the formula in (*24*). In the amorphous carbon regime, $I_D/I_G = C_\lambda' L_a^2$. In the nc-graphite regime, $I_D/I_G = C_\lambda/L_a$. Using a 473-nm excitation laser wavelength, $C_\lambda' \sim 0.00375$ and $C_\lambda \sim 30\,A$ were derived following the method in (*24*, *33*).

Flexible sensor made from laser-ablated HHs

We notice in Fig. 5 (D to F) that flexible devices such as the strain sensor made of laser-ablated carbonaceous materials have distinguishable behaviors. To make reliable devices with linear response to strain, we designed a sandwich structure made of PDMS-ablated electrodes (fig. S8). Both sensors made from ablated tar and laser-ablated MP-asphaltene show a transition between linear regimes with different gauge factor. The strain sensor using laser-ablated tar shows 20× higher gauge factor in both regime, and transition goes up to ~0.06. The enhanced performance in laser-ablated tar could be attributed to three key factors: (i) the paracrystalline graphitic structure with amorphous residual HH induces higher lattice elasticity; (ii) percolated particles in ablated tar form a more stretchable network rather than compact stacked graphite in ablated MP-asphaltene mixture in NMP; and (iii) higher sensitivity of ablated tar to strain results in higher gauge factor. Asphaltene cannot be fully dissolved in NMP, and a physical suspension after stirring (1 hour) in NMP and sonicating (1 hour) is used to coat thin film for strain sensor fabrication.

SUPPLEMENTARY MATERIALS

Supplementary material for this article is available at http://advances.sciencemag.org/cgi/content/full/6/17/eaaz5231/DC1

REFERENCES AND NOTES

1. N. Liu, A. Chortos, T. Lei, L. Jin, T. R. Kim, W.-G. Bae, C. Zhu, S. Wang, R. Pfattner, X. Chen, R. Sinclair, Z. Bao, Ultratransparent and stretchable graphene electrodes. *Sci. Adv.* **3**, e1700159 (2017).
2. S. L. Madorsky, Pyrolysis of hydrocarbon polymers. *Science* **111**, 360–361 (1950).
3. B. D. Keller, N. Ferralis, J. C. Grossman, Rethinking coal: Thin films of solution processed natural carbon nanoparticles for electronic devices. *Nano Lett.* **16**, 2951–2957 (2016).
4. H. Kroto, Space, stars, C_{60}, and soot. *Science* **242**, 1139–1145 (1988).
5. F. D. Mango, The stability of hydrocarbons under the time temperature conditions of petroleum genesis. *Nature* **352**, 146–148 (1991).

6. H. Li, T. Zhu, N. Ferralis, J. C. Grossman, Charge transport in highly heterogeneous natural carbonaceous materials. *Adv. Func. Mater.* **29**, 1904283 (2019).
7. O. P. Morris, X. Zang, A. Gregg, B. Keller, B. Getachew, S. Ingersoll, H. A. Elsen, M. M. Disko, N. Ferralis, J. C. Grossman, Natural carbon by-products for transparent heaters: The case of steam-cracker tar. *Adv. Mater.* **31**, e1900331 (2019).
8. I. Mochida, S.-H. Yoon, N. Takano, F. Fortin, Y. Korai, K. Yokogawa, Microstructure of mesophase pitch-based carbon fiber and its control. *Carbon* **34**, 941–956 (1996).
9. X. N. Zang, C. Jian, T. Zhu, Z. Fan, W. Wang, M. Wei, B. Li, M. F. Diaz, P. Ashby, Z. Lu, Y. Chu, Z. Wang, X. Ding, Y. Xie, J. Chen, J. N. Hohman, M. Sanghadasa, J. C. Grossman, L. Lin, Laser-sculptured ultrathin transition metal carbide layers for energy storage and energy harvesting applications. *Nat. Commun.* **10**, 3112 (2019).
10. J. Lin, Z. Peng, Y. Liu, F. Ruiz-Zepeda, R. Ye, E. L. G. Samuel, M. J. Yacaman, B. I. Yakobson, J. M. Tour, Laser-induced porous graphene films from commercial polymers. *Nat. Commun.* **5**, 5714 (2014).
11. M. H. Studier, R. Hayatsu, E. Anders, Organic compounds in carbonaceous chondrites. *Science* **149**, 1455–1459 (1965).
12. Y. L. Zhang, B. Schuler, S. Fatayer, L. Gross, M. R. Harper, J. D. Kushnerick, Understanding the effects of sample preparation on the chemical structures of petroleum imaged with noncontact atomic force microscopy. *Ind. Eng. Chem. Res.* **57**, 15935–15941 (2018).
13. H. Marsh, C. S. Latham, The chemistry of mesophase formation. *ACS Symp. Ser.* **303**, 1–28 (1986).
14. M. Zander, Aspects of coal tar chemistry/A Review. *Polycycl. Aromat. Comp.* **7**, 209–221 (1995).
15. I. Mochida, S.-H. Yoon, Y. Korai, Mesoscopic structure and properties of liquid crystalline mesophase pitch and its transformation into carbon fiber. *Chem. Rec.* **2**, 81–101 (2002).
16. K. Yano, Y. Itoh, F. Araoka, G. Watanabe, T. Hikima, T. Aida, Nematic-to-columnar mesophase transition by in situ supramolecular polymerization. *Science* **363**, 161–165 (2019).
17. M. R. Narkiewicz, J. P. Mathews, Improved low-volatile bituminous coal representation: Incorporating the molecular-weight distribution. *Energ. Fuel.* **22**, 3104–3111 (2008).
18. G. Malloci, C. Joblin, G. Mulas, Theoretical evaluation of PAH dication properties. *Astron. Astrophys.* **462**, 627–635 (2007).
19. K. O. Johansson, F. El Gabaly, P. E. Schrader, M. F. Campbell, H. A. Michelsen, Evolution of maturity levels of the particle surface and bulk during soot growth and oxidation in a flame. *Aerosol Sci. Technol.* **51**, 1333–1344 (2017).
20. N. Ferralis, Y. Liu, K. D. Bake, A. E. Pomerantz, J. C. Grossman, Direct correlation between aromatization of carbon-rich organic matter and its visible electronic absorption edge. *Carbon* **88**, 139–147 (2015).
21. K. O. Johansson, M. P. Head-Gordon, P. E. Schrader, K. R. Wilson, H. A. Michelsen, Resonance-stabilized hydrocarbon-radical chain reactions may explain soot inception and growth. *Science* **361**, 997–1000 (2018).
22. M. A. Pimenta, G. Dresselhaus, M. S. Dresselhaus, L. G. Cançado, A. Jorio, R. Saito, Studying disorder in graphite-based systems by Raman spectroscopy. *Phys. Chem. Chem. Phys.* **9**, 1276 (2007).
23. P. Milani, M. Ferretti, P. Piseri, C. E. Bottani, A. Ferrari, A. Li Bassi, G. Guizzetti, M. Patrini, Synthesis and characterization of cluster-assembled carbon thin films. *J. Appl. Phys.* **82**, 5793 (1997).
24. A. C. Ferrari, J. Robertson, Interpretation of Raman spectra of disordered and amorphous carbon. *Phys. Rev. B* **61**, 14095 (2000).
25. J. Sjoblom, S. Simon, Z. H. Xu, Model molecules mimicking asphaltenes. *Adv. Colloid Interface Sci.* **218**, 1–16 (2015).
26. C. Jian, S. Merchant, X. Zang, N. Ferralis, J. C. Grossman, Structural evolutions of small aromatic mixtures under extreme temperature conditions: Insights from ReaxFF molecular dynamics investigations. *Carbon* **155**, 309–319 (2019).
27. J. Karweil, in *Chemistry of Coal Utilization*, H. H. Lowry, Ed. (John Wiley & Sons, 1967), vol. 48, pp. 61–85
28. V. A. Davydov, A. V. Rakhmanina, V. Agafonov, B. Narymbetov, J.-P. Boudou, H. Szwarc, Conversion of polycyclic aromatic hydrocarbons to graphite and diamond at high pressures. *Carbon* **42**, 261–269 (2004).
29. Y. Liu, N. Ferralis, L. T. Bryndzia, J. C. Grossman, Genome-inspired molecular identification in organic matter via Raman spectroscopy. *Carbon* **101**, 361–367 (2016).
30. X. H. Fan, Y. Q. Fei, L. Chen, W. Lit, Distribution and structural analysis of polycyclic aromatic hydrocarbons abundant in coal tar pitch. *Energ. Fuel.* **31**, 4694–4704 (2017).
31. O. C. Mullins, H. Sabbah, J. Eyssautier, A. E. Pomerantz, L. Barré, A. B. Andrews, Y. Ruiz-Morales, F. Mostowfi, R. McFarlane, L. Goual, R. Lepkowicz, T. Cooper, J. Orbulescu, R. M. Leblanc, J. Edwards, R. N. Zare, Advances in asphaltene science and the yen-mullins model. *Energ. Fuel.* **26**, 3986–4003 (2012).
32. I. Mochida, Y. Korai, C.-H. Ku, F. Watanabe, Y. Sakai, Chemistry of synthesis, structure, preparation and application of aromatic-derived mesophase pitch. *Carbon* **38**, 305–328 (2000).
33. M. J. Matthews, M. A. Pimenta, G. Dresselhaus, M. S. Dresselhaus, M. Endo, Origin of dispersive effects of the Raman *D* band in carbon materials. *Phys. Rev. B* **59**, R6585–R6588 (1999).
34. D. Pantea, H. Darmstadt, S. Kaliaguine, C. Roy, Electrical conductivity of conductive carbon blacks: Influence of surface chemistry and topology. *Appl. Surf. Sci.* **217**, 181–193 (2003).
35. J. J. Hauser, Hopping conductivity in amorphous carbon-films. *Solid State Commun.* **17**, 1577–1580 (1975).
36. X. N. Zang, C. Shen, Y. Chu, B. Li, M. Wei, J. Zhong, M. Sanghadasa, L. Lin, Laser-induced molybdenum carbide-graphene composites for 3D foldable paper electronics. *Adv. Mater.* **30**, e1800062 (2018).
37. V. Tucureanu, A. Matei, A. M. Avram, FTIR spectroscopy for carbon family study. *Crit. Rev. Anal. Chem.* **46**, 502–520 (2016).
38. S. Coskun, E. S. Ates, H. E. Unalan, Optimization of silver nanowire networks for polymer light emitting diode electrodes. *Nanotechnology* **24**, 125202 (2013).
39. D. C. Glick, A. Davis, Operation and composition of the penn state coal sample bank and data base. *Org. Geochem.* **17**, 421–430 (1991).
40. C. A. Palmer, *The Chemical Analysis of Argonne Premium Coal Samples* (Government Printing Office, 1997), vol. 2144.
41. A. C. T. van Duin, S. Dasgupta, F. Lorant, W. A. Goddard, ReaxFF: A reactive force field for hydrocarbons. *J. Phys. Chem. A* **105**, 9396–9409 (2001).
42. S. Plimpton, Fast parallel algorithms for short-range molecular-dynamics. *J. Comput. Phys.* **117**, 1–19 (1995).
43. W. Humphrey, A. Dalke, K. Schulten, VMD: Visual molecular dynamics. *J. Mol. Graph.* **14**, 33–38 (1996).
44. K. Momma, F. Izumi, VESTA 3 for three-dimensional visualization of crystal, volumetric and morphology data. *J. Appl. Cryst.* **44**, 1272–1276 (2011).
45. Y. Chyan, R. Ye, Y. Li, S. P. Singh, C. J. Arnusch, J. M. Tour, Laser-induced graphene by multiple lasing: Toward electronics on cloth, paper, and food. *ACS Nano* **12**, 2176–2183 (2018).

Acknowledgments

Funding: This work was supported, in part, by ExxonMobil (grant EM09079). Tar can be provided by ExxonMobil Research and Engineering Company (EMRE), with a pending scientific review and a completed material transfer agreement. Requests for tar should be submitted to EMRE. C.J. acknowledges financial support from the Natural Sciences and Engineering Research Council of Canada Postdoctoral Fellowship. This work made use of the MRSEC Shared Experimental Facilities at MIT, supported by the NSF under award number DMR-14-19807. This work used facilities in Center for Nanoscale Systems (CNS) in Harvard University, a member of the National Nanotechnology Coordinated Infrastructure Network (NNCI), which is supported by the NSF under award no. 1541959. CNS is part of Harvard University. **Author contributions:** X.Z., N.F., and J.C.G. designed the research and wrote the paper. X.Z. designed and performed experiments. S.I. and Z.L. helped with device fabrication and testing. J.J.A. synthesized and provided MP pitch and provided insight into the molecular formulation of HH. C.J. performed the simulation. H.L. helped in conceptualizing the simulations. **Competing interests:** The authors declare that they have no competing interests. **Data and materials availability:** All data needed to evaluate the conclusions in the paper are present in the paper and/or the Supplementary Materials. Additional data related to this paper may be requested from the authors.

Submitted 16 September 2019
Accepted 7 February 2020
Published 24 April 2020
10.1126/sciadv.aaz5231

Citation: X. Zang, C. Jian, S. Ingersoll, H. Li, J. J. Adams, Z. Lu, N. Ferralis, J. C. Grossman, Laser-engineered heavy hydrocarbons: Old materials with new opportunities. *Sci. Adv.* **6**, eaaz5231 (2020).